First Observations of Tracking Clouds Using Scanning ARM Cloud Radars.

Paloma Borque[1], Pavlos Kollias[1] and Scott Giangrande[2]

1. Dept. of Atmospheric and Oceanic Sciences, McGill University, Canada
2. Brookhaven National Laboratory, Upton New York

Accepted for publication in J. Applied Meteorol. Clim.
[vol 53, 2732-2746, doi:10.1175/JAMC-D-13-0182.1 (2014)]

Corresponding Author's email: paloma.borque@mail.mcgill.ca

Department of Atmospheric and Oceanic Sciences

Room 945, Burnside Hall, 805 Sherbrooke Street West

Montreal, Quebec H3A 2K6

Tel.: 514-398-1500

Fax: 514-398-6115

Abstract

Tracking cloud entities using scanning cloud radars can help to document the temporal evolution of cloud properties well before large drop formation ("first echo"). These measurements compliment cloud and precipitation tracking using geostationary satellites and weather radars. Here, two-dimensional (2-D) Along-Wind Range Height Indicator (AW-RHI) observations of a population of shallow cumuli (with or without precipitation) from the 35-GHz scanning ARM cloud radar (SACR) at the DOE Atmospheric Radiation Measurements (ARM) program Southern Great Plains (SGP) site are presented. Observations from the ARM SGP network of scanning precipitation radars are used to provide the larger scale context of the cloud field and to highlight the advantages of the SACR to detect the numerous, small, non-precipitating cloud elements. A new Cloud Identification and Tracking Algorithm (CITA) is developed to track cloud elements. In CITA, a cloud element is identified as a region having a contiguous set of pixels exceeding a preset reflectivity and size threshold. The high temporal resolution of the SACR 2-D observations (30 sec) allows for an area superposition criteria algorithm to match cloud elements at consecutive times. Following CITA, the temporal evolution of cloud element properties (number, size, maximum reflectivity) is presented. The vast majority of the designated elements during this cumulus event were short-lived non-precipitating clouds having an apparent lifecycle shorter than 15 minutes. The advantages and disadvantages of cloud tracking using a SACR are discussed.

1. INTRODUCTION

Clouds play a critical role in Earth's climate system through their participation in Earth's radiation budget, the hydrological cycle and the vertical redistribution of energy and moisture in the atmosphere (e.g., Stephens 2005; Feingold and Seibert 2009). The accurate representation of the factors that control cloud microscale and macroscale properties in global climate models (GCMs) and cloud resolving models (CRMs) remains a major challenge (e.g., Ghan et al. 1999; Grenier and Bretherton 2001; Park and Bretherton 2009; Stevens and Feingold 2009). Continuously operating ground-based supersites (Stokes and Schwartz 1994; Ackerman and Stokes 2003; Illingworth et al. 2007) equipped with a wide range of active and passive sensors provide detailed information on cloud dynamical and microphysical properties. Until recently, the cloud properties retrieved at these ground-based supersites were limited to the column sampled by profiling sensors. Now, scanning cloud and precipitation radars are deployed to provide information on the 3D structure of clouds and precipitation (Mather and Voyles 2013; Kollias et al. 2013a). One of the main scientific drivers for deploying scanning cloud radars is the desire to document individual cloud elements as they transit through different stages of their lifecycle (e.g., cloud formation, precipitation onset, dissipation). Relating the temporal evolution of cloud systems to aerosol and large-scale meteorology conditions could lead to a better understanding of the controls on low-clouds and associated statistics.

Monitoring the temporal evolution of shallow cumulus clouds can be accomplished using ground-based and airborne-based radar systems (multiple passes). Capturing the early stage of cumulus development/detection (first echo) depends on the

sensitivity of the radar system. When cm-wavelength radars have been tasked for these studies, the first echo coincides with the early development of small precipitation particles (Knight and Miller 1993; Knight et al. 2002; Göke et al. 2007; Burnet and Brenguier 2010). This early development of a precipitation echo implies that an efficient collision-coalescence process drives particle growth in warm clouds. French et al. (1999) used multiple passes over shallow cumulus clouds and observations from an airborne mm-wavelength radar to document the temporal evolution of non-precipitating cumulus clouds. These early efforts demonstrate the potential of scanning radars to monitor the temporal evolution of shallow cumuli. However, the studied dataset is limited and, in the majority of the studies, the use of cm-wavelength radars does not permit the documentation of the cloud lifecycle before the development of small raindrop particles. The spatial and temporal resolution of geostationary satellites also limits their applicability for the detection of small, non-precipitating cumuli clouds.

The deployment of continuously operating scanning cloud radars (Mather and Voyles 2013; Kollias et al. 2013a) at the US Department of Energy (DOE) Atmospheric Radiation Measurement (ARM) program fixed and mobile sites offers the required observational capabilities for monitoring the entire lifecycle of shallow cumuli clouds over an extensive period of time. This is particularly germane for the ARM Southern Great Plain (SGP) facility that is equipped with a distributed, multi-frequency scanning radar network. This network includes a Scanning ARM Cloud Radar (SACR) with sensitivity (~ -30 dBZ at 10 km) and spatial (45 m) and temporal resolution (~30 sec per horizon-to-horizon scan) sufficient for continuous tracking of non-precipitating short-lived cloud elements.

Here, we present the first set of observations from this scanning cloud radar facility during a warm season cloud event with a wide distribution of cloud types from short-lived, non-precipitating cumuli to shallow, light precipitating cumulus clouds. The details of a Cloud Identification and Tracking Algorithm (CITA) suitable for monitoring the evolution of shallow cumulus in a Range-Height Indicator (RHI) plane are presented. The detection capabilities and observed cloud statistics are compared to those obtained from the scanning ARM precipitation radars. Preliminary statistics of the temporal gradient of the radar reflectivity in shallow non-precipitating clouds are presented. Finally, the limitations and capabilities of the ARM SGP facility to study the lifecycle of cloud elements are discussed.

2. OBSERVATIONS

The observations presented for this study were collected during the Midlatitude Continental Convective Clouds Experiment (MC3E) conducted in April-June 2011 at the ARM SGP facility. MC3E was the result of a collaborative effort between the DOE – ARM program and its Climate Research Facility and the National Aeronautics and Space Administration's (NASA) Global Precipitation Measurement (GPM) mission Ground Validation (GV) program. The MC3E campaign was the first major field experiment conducted at an ARM site after the acquisition of the new scanning ARM radar (Fig. 1, Mather and Voyles 2013). The backbone infrastructure of the ARM SGP radar facility is a distributed, heterogeneous network of profiling and scanning radar systems suitable for the mapping of cloud and precipitation in 3D along with a small network of radiometers and lidars. The SGP radar facility includes a 5.4-GHz (5.5 cm wavelength) C-band Scanning ARM Precipitation Radar (C-SAPR), a network of three 9.4-GHz (3.2 cm wavelength) X-band Scanning ARM Precipitation Radars (X-SAPR), and a dual-frequency 35.3/93.9-GHz (8.5/3.2 mm) Scanning Cloud Radar (Ka-/W- SACR – Fig. 1).

The bulk of the observations presented in this manuscript are from the SACR located in the Central Facility (CF). A Total Sky Imager (TSI), radiosonde launch facility, 2-dimensional video disdrometer, wind profiler, and a laser ceilometer are also present at the CF and are used in this study. The C-SAPR is located approximately 25 km to the north of the SGP-CF and the three X-SAPR systems are located in a triangular configuration having a side (baseline) of approximately 20 km and centered on the SGP-CF (Fig. 1). The primary motivation for the C-SAPR polarimetric radar system is to provide the mesoscale context of precipitation over a 100-120 km domain range around

the CF. The acquisition of the X-band radar network at the ARM SGP radar facility is based on the desire to bridge the observational gap in sensitivity and spatial scales between the dual-frequency scanning cloud radar and C-band polarimetric radar. The SACR is a dual frequency scanning Doppler and polarimetric radar. However, during the MC3E only the 35-GHz (Ka-band) radar frequency was operational (Table 1). With sensitivity close to -30 dBZ at 10 km during nominal scanning parameters, the Ka-SACR is capable of detecting clouds from their early formation stages. SACR scan strategies for this event included horizon-to-horizon Along-Wind scans (AW-RHI), which requires the primary wind direction at cloud level as an input. Once the wind direction is designated, the cloud radar is expected to capture the evolution of the same cloud element as it is advected over the instrument. For this particular case, the wind direction was determined by consulting the relevant 1730 UTC radiosonde, wind profiler and visible satellite imagines available in real time by the authors in the field. This wind direction was visually confirmed in-situ by the authors and later corroborated by the 2030 UTC radiosonde also launched at the CF. The scan direction was fixed for the duration of the Ka-SACR AW-RHI scan strategy period. This was not a major concern since, during this 2.5-hour interval, wind in the cloud layer did not have an appreciable change in time or height and there was not a distinguishable shear that could cause clouds to move differently at different heights (Fig. 2). Furthermore, later inspection of the X- and C-SAPR data showed that the motion field of clouds detected by these systems did not differ substantially from the previously assumed flow (not shown). Once the wind direction was determined, the SACR azimuth was aligned to this mean cloud layer wind direction and the radar was tasked to perform long sequences of horizon-to-horizon AW-

RHI scans to capture the evolution of the same cloud elements as they propagate towards, over and away from the SACR. Additional details on the first generation of SACR operational strategies and data post-processing are described in Kollias et al. (2013a, b).

Figure 3 demonstrates the advantage of using a heterogeneous network of radars to document the temporal and spatial distribution of clouds from their early, low reflectivity stages to their more mature precipitation-associated regime and following lower reflectivity decay stage. Here an example of data collected by the Ka-SACR, C-SAPR and the SE X-SAPR at a time for which primarily weak, non-precipitating clouds were present over SGP-CF is shown. The Total Sky Imager (Fig. 3a) confirms the presence of shallow, broken cumuli over the CF. These same clouds are observed by the Ka-SACR overhead (Fig. 3d). All ARM radars observe a precipitating shallow cumulus at a 5-10 km range from the Ka-SACR (southeast part of the AW-RHI scan). However, the SAPRs have difficulty detecting the non-precipitating clouds observed by the Ka-SACR illustrating the importance of millimeter radar observations for capturing shallow non-precipitating clouds as well as the early stages of cloud evolution (Fig. 3). This is not only due to differences in wavelength but also, in a smaller manner due to beam width, relative cloud-to-radar distance and scanning strategy [Add References].

3. CLOUD IDENTIFICATION AND TRACKING ALGORITHM

The literature provides many examples of studies that have sought to follow the evolution of cloud systems, with the most salient examples considering the lifecycle and morphology of deep convective systems through the use of cloud-tracking algorithms (e.g., Williams and Houze 1987; Velasco and Fritsch 1987; Rosenfeld 1987; Johnson et al. 1998; Dixon and Wiener 1993; Machado et al. 1998). Satellite-based cloud tracking studies identify deep convective cloud elements using infrared temperature (T_{IR}) thresholds (e.g., Maddox 1980; Williams and Houze 1987; Chen et al. 1996) and additional spatial coherency constraints (e.g., Machado et al. 1998; Futyan and Del Genio 2007). From the surface, radar-based cell designation and tracking algorithms capitalize on radar reflectivity factor patterns and additional size constraints (e.g., Dixon and Wiener 1993; Rosenfeld 1987; Johnson et al. 1998). These radar-based 'cell' identification efforts then act as input for tracking algorithm components that analyze the evolution of these cell patterns by determining area superposition between consecutive time steps (e.g., Williams and Houze 1987; Boer and Ramanathan 1997; Machado et al. 1998), cloud propagation speed and superposition (Rosenfeld 1987; Johnson et al. 1998; Futyan and Del Genio 2007), or by minimizing a cost function based on position and element volume differences at consecutive times (e.g., Dixon and Wiener 1993). For such deep convective cells and larger convective system examples, automatic and semiautomatic (manual selection of the optimal candidate) tracking algorithms often arrive at similar results (e.g., Machado et al. 1998).

The Cloud Identification and Tracking Algorithm (CITA) is developed to analyze shallow cumulus clouds as they transit through different stages of their lifetime. The

input to CITA is 2-D (range-height) Ka-SACR observations collected during an AW-RHI scan (e.g., Fig. 3d). Range gates that contain no meteorologically significant detections have been removed using a SNR threshold technique (e.g., Kollias et al. 2013b). Furthermore, conditional sampling using the Linear Depolarization Ratio (LDR) and radar reflectivity from the Ka-SACR, as well as the cloud base height from a ceilometer, has been applied to classify and filter radar echoes associated with insects (Kollias et al. 2013b). Once these non-meteorological radar returns are removed, each AW-RHI radar image is processed and CITA identifies a cloud element as those echoes having a contiguous set of pixels with reflectivity greater or equal than -50 dBZ and assign them an identification number (ID). The reflectivity of -50 dBZ matches the Ka-SACR sensitivity at a 1-km range during nominal scanning operational conditions. Although the Ka-SACR will not be able to detect such weak cloud echoes at longer distance from the radar, it is known that the Ka-SACR still offers sufficient sensitivity to observe weak, non-precipitating clouds at extended range. To eliminate spurious echo clusters (due to imperfect removal of radar noise-only range gates and insect returns), only those radar echo clusters having areal coverage larger than 0.5 km^2 are considered as cloud elements.

The second step within CITA is to apply a superposition criterion to track the temporal-spatial movement of each ID assigned cloud element (Fig. 4b-c). The superposition criterion identifies clusters that have the largest areal overlap in consecutive radar scans and links them as echoes coming from the same cloud. This assumption is considered reasonable for the AW-RHI SACR scans that were generated every 30 seconds during this campaign. When two cloud elements merge, the larger element is considered to continue and the smaller to terminate. Similarly, when a cloud

element splits, the larger element continues with the previously assigned tracking ID and the smaller appears as a new element. Validation for merges and splits detected by CITA was done by time coherency in the range-height plane (this was determined by the authors by visually inspecting every RHI scan from the SACR) and areal thresholds to mitigate the weakest cloud features that may result from poor cumulus cloud RHI slicing.

An example application of CITA for a sequence of three consecutives along-wind scans from Ka-SACR on 25 May 2011 is shown in Fig. 4. At the first time step, six cloud cells are identified by CITA (ID: 1-6). Cloud elements having the tracking IDs 1 and 4 demonstrate an undisturbed lifecycle with no merges or splits during the provided sequence (Fig. 5), whereas cloud elements assigned the IDs 2 and 3 (Fig. 4a) merge into a single cloud element assigned to tracking ID 2 (Fig. 4b), and cloud ID 6 (Fig. 4b) splits into two cloud elements with IDs 6 and 7 (Fig. 4c). A more in depth analysis of this complex time sequence is shown later in this section. For this observing period, the aforementioned criteria were applied for the large majority of the cases successfully, as confirmed by visual inspection by the authors. This success of the echo overlap criteria eliminates the need to explore more computationally demanding approaches that require the estimation of the propagation speed, or the minimization of a cost function based on position and volume to assess the best possible match for every cloud element. Several tests were performed to evaluate the robustness of CITA results. Firstly, identified cloud elements and associated evolution were manually inspected and verified by the authors. Secondly, a simple test of algorithm repeatability was performed, the CITA approach was applied to this dataset in reverse temporal order, with the CITA demonstrating very similar ID counts and tracking results. Thirdly, the sensitivity of CITA to different

detection thresholds was also tested for this event. The analysis indicated that for reflectivity thresholds between -40 and -50 dBZ, there was no significant change with the number of clouds detected by the CITA approach or in the associated cloud primary microphysical or geometrical proprieties (Fig. 5). However, if more restrictive threshold changes were applied (e.g., higher reflectivity thresholds were selected), the impact on tracking and evolution behaviors became more noticeable, as anticipated in light of past radar and satellite tracking studies. One noteworthy consideration for the feedback between reflectivity thresholds and CITA results was found when exploring the implication of higher reflectivity thresholds on the documentation of the maximum cloud element reflectivity. Specifically, single cloud elements often exhibit multiple maxima regions, most likely attributed to coherent precipitation shafts that are embedded within lower regions of cloud element reflectivity. When more restrictive thresholds (closer to classical values for the presence of drizzle particles ~ -10 dBZ) are applied, these multi-core cloud elements are often reclassified into unique cloud entities rather than grouped as a single cloud element. Since our study emphasizes the analysis of individual cloud elements regardless of the number of interior precipitation cores, the behaviors associated with thresholds closer to -50 dBZ seem to be the most appropriate to track singular cloud features. However, this low reflectivity threshold can also presents challenges in the interpretation of the output from CITA. Further inspection of a longer time sequence of the clouds shown in figure 6 shows how complex the identification and tracking algorithm can really be. As an example, when considering previous time steps, it can be seen that IDs 2, 4 and 6 developed with their top capped at 2.5km as early as 19:40UTC. These cloud elements then individually merged with other cloud elements that originate

later in time. These higher clouds present a cloud-top height at around 4.5km and seem to have a vertically extent of 1km approximately (as can be seen from figure 4c). The problem with the low reflectivity threshold is that later in time these cloud elements tend to separate, or split, again, and what one could interpret as a cloud that developed on top could be analyzed as a two cloud entities that merged and later split, but if a more restrictive threshold is applied then some clouds might not outlive the size threshold and loose their initiation and/or decay moments and some of the statistics will be biased towards larger and deep clouds. Therefore, it is a trade-off between fully capturing cloud entities (and their edges and 'deeper cells' embedded in them as part of it and not separate entities) and being able to perfectly and unambiguously distinguish between different cloud entities at every time step in an automatic way. We believe that this type of analysis and algorithm, if wants to be used independently of the case and in an automated way, should be used with a large enough dataset and in a statistical way to smooth out the possible biases introduced by the chosen reflectivity threshold since it was shown that, in a statistical way the main variables analyzed here are not very sensitive to the selected threshold (Fig. 5).

4. RESULTS

Using Ka-SACR observations from the 25 May 2011, CITA identified a total of 1323 individual cloud elements, 49 of them (3.7%) were the result of a merge and 50 (3.78%) of a split, and tracked the lifecycle of 338 distinct cloud elements (Fig. 6). Therefore, the lifecycle of the vast majority of the cloud elements identified and tracked by CITA mainly correspond to undisturbed and continuous evolution of cloud elements with only one unique link at each time step of their lifecycle. In particular, three long-lived shallow cloud elements (having cloud tops below 5 km) tracked by the Ka-SACR CITA during this period persisted for more than 25 minutes. These clouds attained maximum reflectivity values exceeding 20 dBZ during most of the observed cloud lifecycle and exhibited cross-sectional areas in excess of 40 km^2 (Fig. 6). The majority of the shallow cloud elements observed however, were short-lived features with CITA tracking lifecycles under 10 minute and low maximal reflectivity cores (below -5 dBZ, see Figs. 6 and 7). Most often, weaker cloud elements are observed to have dissipated (or exited the domain) after less than 5 minutes of their first detection. The validity that these features are legitimate scans from shallow cloud elements (separate from 'detrained' cloud elements in a sheered flow) was confirmed by author in-field observations and sounding evidence, surface TSI camera imagery, as well as the absence of stronger echoes in the SAPRs imagery near the cloud radar scanning transect during most periods of observation.

It is important to note that there is a likely underrepresentation in these statistics due to the radar scans not sampling the center of the cloud. Jorgensen et al. 1985 found a diameter bias of approximately 22% when sampling spherical updraft cores from aircraft.

This circular shape assumption for cumulus clouds may be applicable under low shear conditions (such as the ones present during most of the time in this event, e.g. fig.2) however; it might not be applicable for all the cloud lifecycle. Here we extended this analysis to a generic ellipsoidal shape of cloud elements. As expected, biases for more elongated cloud are more pronounced. For example, if clouds are elongated along the wind direction having an axis ratio (major to minor dimension) of 0.8, the expected bias in areal coverage would be roughly 32%. This suggests that future scan strategies should include low-level PPI scans to effectively capture the structure of clouds and help establish the placement of future AW-RHI.

The distribution of the maximum radar reflectivity values determined for all 338 cloud elements detected within the Ka-SACR sampling period is offered in Fig. 7a. This plot indicates that the majority of the cloud elements attain a maximum radar reflectivity between -20 to -10 dBZ (Fig. 7a). This magnitude of radar reflectivity at the SGP location in central Oklahoma is consistent with clouds that do not produce drizzle (Lu et al., 2008). The frequency distribution of maximum horizontal-height area coverage attained by all cloud elements peaks at the smallest-possible detectable area coverage for CITA methods (0.5 km^2).

Additional geometrical properties for the identified cloud elements are also documented by CITA as a function of time. These parameters include the number of cloud elements, the cloud element top height and the maximum horizontal length of the cloud elements. The behaviors of these fields observed by the Ka-SACR for the 25 May event are provided in Fig. 8. During times of precipitation in the vicinity of the cloud radar (approximately 1920 UTC, 1950 UTC and 2040 UTC, Fig. 8e disdrometric

observations at SGP – CF and C-SAPR estimations in a larger domain), there are a few cumulus cloud elements (Fig. 8b) with extended horizontal lengths (Fig. 8c) and higher relative top heights (Fig. 8d). In contrast, there is a suggestion of a strongly bimodal or occasionally more complex distribution of cloud-top heights, most having shorter cumulus horizontal length scales, within the non-precipitating and weaker initiating times. During these sequences that include times at the beginning of the observation period, one can consistently observe clouds having tops ranging from the lower levels around 1.5 km (in association with the top of the boundary level) up to higher cloud top levels near 3.5 km (in association with the freezing level), within the same scan. Yet, when considering the periods associated with the onset or nearby precipitation, the complexity of these tracked parameters is often reduced and cloud tops below 1.5km disappear letting it mainly characterized by cloud elements with elevated tops. A plausible explanation for this distribution relates to the evolution of the cloud field and its associated dynamics. This event started with exclusively shallow cumulus clouds that later transitioned to congestus clouds with some shallow cumulus still present in the region. Therefore, the multilevel cloud top structure is likely to be a combination of very shallow, non-precipitating mode, with some deeper precipitating cumulus with entrainment at multiple levels. However, it is likely that in times when congestus clouds dominate the near vicinity of the radar (approximately 1920 UTC, 1950 UTC and 2040 UTC) its associated cold pool-type outflow (noticeable from the drop in equivalent potential temperature at SGP – CF, Fig. 8c) effectively act in a capacity to deter lower-topped shallow, surface forced convection and temporarily reduces those observations for an extended windows of atmospheric recovery.

As a preliminary attempt to explore time-evolving cloud maximum and median properties and the associated local rate of change (as potentially related to cloud microphysical process and cloud growth and decay therein) the evolution of cloud radar reflectivity fields from discrete shallow, non-precipitating cloud target examples are provided in Fig. 9. To ensure these discrete, non-precipitating cumuli conditions, the maximum and median parameter calculations and associated rate of change estimates are limited to only those calculations from the individual cloud elements that persist for a minimum of 5 minutes and have a maximum radar reflectivity that does not exceed -5 dBZ during the CITA cloud lifecycle tracking. As an additional constraint, we restrict the dataset to only those pure or discrete cloud elements for which the CITA IDs have not experienced a merge or a split. Finally, the remaining clouds are checked to ensure that a maximum in the radar reflectivity factor in time occurs at least three time steps after (before) the initial (final) detection by CITA. This latter constraint is intended to mitigate the inclusion of clouds that either initiate too close to the edge of the Ka-SACR scanning domain and might propagate out of the domain before achieving a mature state or mature clouds entering the edge of the scanning domain for which initiation or growth stages are not captured.

For these Fig. 9 demonstrations, it is observed that the local growth and/or decay rates of the maximum reflectivity are typically less than 10 dBZ/minute and exhibit no clear relationship between the maximum reflectivity and its local rate of change for the surrounding minute of radar observations (Figs. 9a-b). Median cloud reflectivity values and the associated local rates of change are more gradual and demonstrate a maximum of 5 dBZ/minute (Figs. 9c-d). Similarly, the local rate of change is likely to be independent

of the median reflectivity value. In contrast to the maximum, the median value and its relationship to its local rate of change is shown to be strongly tied to relative location of the cloud element to the radar location, wherein lower magnitudes of the median are observed closer to the radar location (Figs. 9b-d). This is an obvious consequence of cloud elements having reduced radar sensitivity with range due to increased range gate volume with distance from radar. The influence of radar sensitivity is larger if considering the evolution of the mean cloud reflectivity and its local rate of change (not shown). This indicates a limited relationship between these parameters and their rate of change, thus showing the larger influence of radar sensitivity when analyzing the time evolution of the mean and median cloud reflectivity.

5. Discussion and Conclusions

This manuscript offers preliminary findings towards the potential capability to track and document the lifecycle of shallow and weak cumulus to drizzling and showery cumulus clouds using a scanning millimeter wavelength cloud radar. Whereas cloud radars typically exhibit enhanced sensitivity for the detection of these low-level cloud features, the ability of the Scanning ARM Cloud Radar (SACR) mm-wavelength radar for detection of the particular shallow and non-precipitating boundary layer clouds from this dataset was improved owing to a reduced signal-to-clutter ratio and suppressed coherent scattering (e.g., Kollias et al., 2007). An AW-RHI scan strategy was implemented during the MC3E campaign and included high temporal sampling to facilitate the following of transient cloud elements as they advect with the mean wind field over the SACR platform at the ARM Southern Great Plains – Central Facility (SGP – CF). The ARM SGP site during the MC3E campaign was home to a network of complementary scanning precipitation radars, lidar and collocated surface cloud properties instrumentation that gave context to SACR observations. Simple morphological analysis of complementary reflectivity factor observations from the scanning radar facilities in particular helps demonstrate the potential benefits for having multi-wavelength radar facilities of various scanning coverage scales, or cloud observational 'supersites', to help bridge gaps between different cloud scales. There are significant morphological implications when one is unable to capture the full dynamic range of clouds from the smallest scales that may be detected by the millimeter wavelength radar (SACR) to the larger scales covered by the centimeter radars (X- and C-SAPR).

To better demonstrate the capabilities of the ARM SACR systems for the documentation of shallow cumulus evolution, a radar-based tracking algorithm (Cloud Identification and Tracking Algorithm – CITA) was developed. A goal for CITA was to explore the possibilities for a functional method to track key cloud microphysical and geometric parameters, including their evolution in time and space, which are of interest to detailed cloud process studies and cloud model evaluation. Basic sensitivity testing for our initial set of CITA parameter outputs revealed that the current CITA design is capable of reliably documenting cloud metrics, such as cloud element counts, maximum radar reflectivity factor and cloud geometric properties including cloud top and cross-sectional area. CITA was tested on a postfrontal shallow cumulus dataset collected by the SACR when performing along-wind scans during MC3E on 25 May 2011. This day exhibited a wide variety of cumulus cloud conditions and featured two and one half hours of uninterrupted rapid radar scanning rates thereby allowing CITA to track clouds unambiguously with time (e.g., Figs. 6, 7). The vast majority of the cloud elements detected by CITA were short-lived with lifecycles shorter than 15 minutes, most of them decaying after the first 5 minutes and exhibiting low maximal reflectivity cores.

Three long-lived cumulus clouds were captured during the collection period and attained high reflectivity values that can be associated with precipitation onset in the region. The associated time evolution captured by CITA is complex, yet potentially highlights the eventual suffocation of the previously surface driven-sort shallow cumulus clouds (albeit, those having additional larger-scale forcing in the post-frontal environment) in the vicinity of the Ka-SACR. Moreover, observations suggest that these deeper precipitation modes preceded sequences of higher-based non-precipitating

cumulus cloud over the site, with these higher based clouds possibly influenced by downward mixing of dry air associated with the preceding precipitation over or near the region. Overall, most precipitation-free times demonstrate interesting behaviors during the presented event, including bimodal or more complex distributions of low-level cumulus clouds in terms of cloud-top heights and of smaller relative horizontal lengths.

Additional interpretation of the CITA dataset outputs in the context of the 25 May 2011 MC3E event indicates most cloud elements reflect numerous shallow, non-precipitating clouds having a maximum radar reflectivity lower than -5 dBZ (near the traditional "first echo" limit of precipitation radars). These shallow cumuli were often observed to be short-lived. The time-varying behaviors of the maximum and median cloud reflectivity and local attempts to calculate associated rates of change for non-precipitating shallow cumulus examples were less conclusive (e.g., Fig. 9). It is not surprising to note that in following the evolution of median (and mean) cloud element reflectivity factors, the tracking must account for changes in the sensitivity of the radar to cloud echoes to be of much use. Nevertheless, following cloud maximum behaviors (less influenced by radar sensitivity issues) as tractable quantities for microphysical evolution of the clouds was also challenging to interpret, as echo maximums are found to evolve quite rapidly and significantly in magnitude for well-captured shallow, non-precipitating cloud echo elements and within only a few minutes of observation.

As this is the first application of CITA, more datasets are needed to drive a more robust verification of the CITA methodology and to allow more comprehensive cloud statistics. The findings for this study are also limited to shallow cloud observations from the Oklahoma SGP ARM facility, although we anticipate the methods should translate

well to other ARM facilities for similar low cloud conditions. Application of CITA in real-time or field campaign settings is also however nontrivial and strongly tied to an ability to characterize the cloud-level winds and appropriately (and repeatedly) target the same cloud elements in time that are assumed to propagate along that mean wind direction. Highly variable wind with time and, in the case of larger more vigorous clouds, cloud development/decay alignment can play a role in a successful implementation of this methodology as a fully automated tracking system. While those assumptions for most cloud types are likely viable, tracking algorithm design problems may be exacerbated by the narrow beamwidth of the Ka-SACR (0.3°) and other similar cloud radar systems. Moreover, for such small beamwidths, only very small errors when establishing a mean horizontal wind direction could affect substantial decreases in the quality and continuity of the measurements, additional details on the sensitivity to the horizontal wind direction is described in the appendix. Specifically, this suggest that several clouds would not likely follow a path over the radar site and therefore represent an eventual inability for the radar to track the complete (or best-case partial) evolution of valid cloud elements with time. Different scanning strategies (including routine or reference sector scans) can mitigate some of these known difficulties (e.g., Boundary Layer – RHIs, additional details on scan strategies are described in Kollias et al. 2013a). However, utilizing these scans implies a tradeoff between the scanning necessary for adequate temporal revisit of cloud elements for tracking and microphysical process monitoring as compared to the needs to assure the individual clouds are properly captured or tracked in full spatial contexts.

8. Acknowledgements

The authors wish to thank the reviewers whose insightful comments and suggestions enhance this manuscript. This manuscript has been authored by employees of Brookhaven Science Associates, LLC under Contract No. DE-AC02-98CH10886 with the U.S. Department of Energy. The publisher by accepting the manuscript for publication acknowledges that the United States Government retains a non-exclusive, paid-up, irrevocable, world-wise license to publish or reproduce the published form of this manuscript, or allow others to do so, for United States Government purposes. Dr. Giangrande's work is supported by the U.S. Department of Energy, Office of Science, Office of Biological and Environmental Research (OBER) as part of the ASR and ARM programs. Additional author support was provided by the US DOE Atmospheric System Research (ASR) program and by the BNL Laboratory Directed Research and Development (LDRD) Program.

Appendix

The success of CITA partially depends on the accurately determination of the environment wind direction for the set up of the along-wind scan strategy (AW-RHI). This is extremely dependent on the wind field and the cloud lifetime. In this particular case, the wind field is not expected to significantly influence the results since it did not present an appreciable change in time or height and there was no distinguishable shear that could cause clouds to move differently at different heights. Considering a very simple advection model the deviation from the wind direction that the AW-RHI scan strategy can have and still sample the same volume will mostly depend on the size of the region that is assumed homogeneous, the wind speed at which clouds propagate and cloud lifecycle. Due to the Ka-SACR beamwidth at a 10km distance from the radar the sampling volume is approximately a cylinder of ~50m diameter, considering this to be the size of the region to be homogeneous, assuming a constant horizontal wind and that cloud elements are advected over the radar domain with the middle point of their lifecycle occurring over the location of the radar then the estimation of the maximum deviation of the radar scan angle from the wind direction can be estimated (Fig. 10). Small errors in the horizontal wind direction could substantially impact the use of this technique, for this particular case study, considering wind speeds slower than 20 m/s (Fig. 2) and cloud lifetime shorter than 10 minutes (Fig. 6), the same cloud volume will be sampled approximately 20 times and capture the evolution of the same parcel only if there is a variation of 1 degree between the scan angle and the wind direction. However, considering a slower advection speed of 10m/s and shorter cloud lifecycles then the

disagreement between the cloud propagating and scan angle can be close to 5 degrees and still sample proprieties within the same volume, and of course considering a larger parcel size will also modify these results by allowing a larger disagreement between the angles (i.e., if assuming a homogeneous volume with diameter of 100m, the deviation between the angles can be almost doubled).

6. REFERENCES

Ackerman, T. A., and G. M. Stokes, 2003: The Atmospheric Radiation Measurement Program. *Phys. Today*, **56**, 38–45.

Boer, E., and V. Ramanathan, 1997: Lagrangian approach for deriving cloud characteristics from satellite observations and its implications to cloud parameterizations. *J. Geophys Res.,* **102**, 21383-21399

Burnet, F., and J.-L. Brenguier, 2010, The onset of precipitation in warm cumulus clouds: An observational case-study. *Q.J.R. Meteorol. Soc.*, **136**, 374–381. doi: 10.1002/qj.552

Chen, S. S., and B. E. Mapes, 1996: Multiscale variability of deep convection in relation to large-scale circulation in TOGA COARE. *J. Atmos. Sci.*, **53**, 1380–1409.

Dixon, M., and G. Wiener, 1993: TITAN: Thunderstorm Identification, Tracking, Analysis, and Nowcasting—A radar-based methodology. *J. Atmos. Oceanic Technol.,* **10**, 785–797.

Feingold, G., and H. Siebert, 2009: *In Clouds in the Perturbed Climate System: Their Relationship to Energy Balance, Atmospheric Dynamics, and Precipitation*. J. Heintzenberg, and R. J. Charlson, eds., Strüngmann Forum Reports, **2**, The MIT Press, 597 pp.

French, J. R., G. Vali, and R. D. Kelly, 1999: Evolution of small cumulus clouds in Florida: Observations of pulsating growth. *Atmos. Res*, **52**:143–165.

Futyan, J. M., and A. D. Del Genio, 2007: Deep Convective System Evolution over Africa and the Tropical Atlantic. *J. Climate*, **20**, 5041–5060.

Ghan, S. J., L. R. Leung, J, and McCaa, 1999: A Comparison of Three Different Modeling Strategies for Evaluating Cloud and Radiation Parameterizations. *Mon. Wea. Rev.*, **127**, 1967–1984.

Giangrande, S.E., S. Collis, A. Theisen, and A. Tokay, 2013; Precipitation Estimation from the ARM Distributed Radar Network During the MC3E Campaign. *Submitted, J. Appl. Meteorol. and Climatol*.

Göke, S., H. T. Ochs, and R. M. Rauber, 2007: Radar Analysis of Precipitation Initiation in Maritime versus Continental Clouds near the Florida Coast: Inferences Concerning the Role of CCN and Giant Nuclei. *J. Atmos. Sci.*, **64**, 3695–3707.

Grenier, H., and C. S. Bretherton, 2001: A Moist PBL Parameterization for Large-Scale Models and Its Application to Subtropical Cloud-Topped Marine Boundary Layers. *Mon. Wea. Rev.*, **129**, 357–377.

Illingworth, A. J., R. J. Hogan, E. J. O'Connor, D. Bouniol, M. E. Brooks, J. Delanoe, D. P. Donovan, J. D. Eastment, N. Gaussiat, J. W. F. Goddard, M. Haeffelin, H. Klein Baltink, O. A. Krasnov, J. Pelon, J.-M. Piriou, A. Protat, H. W. J. Russchenberg, A. Seifert, A. M. Tompkins, G.-J. van Zadelhoff, F. Vinit, U. Willen, D. R. Wilson, and C. L. Wrench, 2007. *Bull. Am. Meteorol. Soc.*, **88**, 883-898.

Johnson, J. T., P. L. MacKeen, A. Witt, E. D. Mitchell, G. J. Stumpf, M. D. Eilts, and K. W. Thomas, 1998: The storm cell identification and tracking algorithm: An enhanced WSR-88D algorithm. *Wea. Forecasting*, **13**, 263–276.

Jorgensen, D. P., E. J. Zipser, M. A. LeMone, 1985: Vertical Motions in Intense Hurricanes. *J. Atmos. Sci.*, **42**, 839–856.

Knight, C. A., and L. J. Miller, 1993: First radar echoes from cumulus clouds. *Bull. Amer. Meteor. Soc.*, **74,** 1179–1193

Knight, C. A., and L. J. Miller, 1998: Early radar echoes from small, warm cumulus: Bragg and hydrometeor scattering *J. Atmos. Sci.*, **55,**2974–2992

Knight, C. A., J. Vivekanandan, and S. G. Lasher-Trapp, 2002: First Radar Echoes and the Early ZDR History of Florida Cumulus. *J.Atmos. Sci.*, **59**, 1454–1472

Kollias P., N. Bharadwaj, K. Widener, I. Jo, and K. Johnson, 2013a: Scanning ARM Cloud Radars - Part I: Operational Sampling Strategies. In review to *J. Atmos. Oceanic Technology*.

Kollias P., I. Jo, P. Borque, A. Tatarevic, K. Lamer, N. Bharadwaj, K. Widener, K. Johnson, and E. E. Clothiaux, 2013b: Scanning ARM Cloud Radars – Part II: Data Quality Control and Processing. *In review to J. Atmos. Oceanic Technology*.

Kollias, P., E. E. Clothiaux, A. A. Miller, B. A. Albrecht, G. L. Stephens, and T.P. Ackerman, 2007: Millimeter-wavelength radars: New frontier in atmospheric cloud and precipitation research. *Bull. Amer. Meteo. Soc*., **88**: 1608-1624. doi: 10.1175/BAMS-88-10-1608.

Lu, M.-L., G. Feingold, H. H. Jonsson, P. Y. Chuang, H. Gates, R. C. Flagan, and J. H. Seinfeld, 2008, Aerosol-cloud relationships in continental shallow cumulus, *J. Geophys. Res.*, **113**, D15201, doi:10.1029/2007JD009354.

Machado, L. A., W. B. Rossow, R. L. Guedes, and A. W. Walker, 1998: Life cycle variations of mesoscale convective systems over the Americas. *Mon. Wea. Rev.*, **126**, 1630–1654.

Maddox, R. A., 1980: Mesoscale convective complexes. *Bull. Amer. Meteor. Soc.*, **61**, 1374–1387.

Mather, J. H., and J. W. Voyles, 2013: The Arm Climate Research Facility: A Review of Structure and Capabilities. *Bull. Amer. Meteor. Soc.*, **94**, 377–392. doi: http://dx.doi.org/10.1175/BAMS-D-11-00218.1

Park, S., and C. S. Bretherton, 2009: The University of Washington Shallow Convection and Moist Turbulence Schemes and Their Impact on Climate Simulations with the Community Atmosphere Model. *J. Climate*, **22**, 3449–3469.

Rosenfeld, D., 1987: Objective method for analysis and tracking of convective cells as seen by radar. *J. Atmos. Oceanic Technol.*, **4**, 422–434.

Stephens, G. L., 2005: Cloud Feedbacks in the Climate System: A Critical Review. *J. Climate*, **18**, 237–273. doi: http://dx.doi.org/10.1175/JCLI-3243.1

Stevens, B., and G. Feingold, 2009: Untangling aerosol effects on clouds and precipitation in a buffered system, *Nature* **461**, 607-613

Stokes, G. M., and S. E. Schwartz, 1994: The Atmospheric Radiation Measurement (ARM) Program: Programmatic background and design of the cloud and radiation testbed. Bull. Amer. Meteor. Soc., **75**, 1201–1221.

Velasco, I., and J. M. Fritsch, 1987: Mesoscale convective complexes in the Americas. *J. Geophys. Res.*, **92**, 9591–9613.

Williams, M., and R. A. Houze, 1987: Satellite-observed characteristics of winter monsoon cloud clusters. *Mon. Wea. Rev.*, **115**, 505–519.

Scanning ARM Cloud Radar (Ka-band)	
Scan type	Along-Wind Horizon-to-Horizon
Nyquist velocity	10.5 ms^{-1}
Range resolution	20 m
Scan time	~30 sec
PRF	5 kHz
Sensitivity	~ -30 dBZ at 10 km
Frequency	35.29 GHz
Wavelength	8.5 mm

Table 1: Ka-band Scanning ARM Cloud Radar (Ka-SACR) technical specifications

7. FIGURE CAPTIONS

Figure 1. Map showing the heterogeneous ARM radar network at the SGP facility. Blue rings indicate a 20 km radius around each X-band radar and red ring indicates a 30 km radius around the C-band radar.

Figure 2. Wind magnitude (a) and direction (b) from radiosonde observations at SGP – CF at 1730 UTC (blue) and 2030 UTC (black) on 25 May 2011.

Figure 3. Hemispherical view of the cloud field at the Central Facility from the Total Sky Imager (a), reflectivity from the C-SAPR at 2011 UTC (b), X-SAPR at 2010 UTC(c) PPI scan at 1.2° and 1.5° respectably and from Ka-SACR AW-RHI scan at 2010 UTC (d) on 25 May 2011 when weak non-precipitating cloud were present over the Central Facility. Blue triangle represents the location of the radar and white dot represents the location of the Central Facility; on panels (b) and (c) black line represents the SACR scan and black circle represents the domain where SE X-SAPR data are collected. Orientation in panel d) is NW on the right and SE on the left.

Figure 4. Reflectivity from three consecutive Ka-SACR along-wind scans from 19:44 to 19:45 UTC (shaded) and cloud's identification number documented by the CITA (Contour). Radar location is depicted by the yellow rectangle and the time of each scan is indicated in the bottom left sector of each sub-panel.

Figure 5. Maximum reflectivity frequency (bin: 2 dB, upper panel) and cloud area cross-section frequency (bin: 0.5 km2, lower panel) for different reflectivity detections threshold in the Cloud Identification and Tracking Algorithm for the 25th May 2011 case.

Figure 6. Cross-sectional area (a) and maximum reflectivity (b) as a function of time for every element detected by the CITA on 25 May 2011 during the 2.5-hour window. Colors represent individual clouds tracked by CITA.

Figure 7. Histogram of maximum reflectivity (a) and area (b) of all cloud elements detected by CITA for the 25 May 2011 case.

Figure 8. A sequence of TSI images during the 2.5-hour long observing period (a), the number of cloud elements observed in the Ka-SACR AW-RHI scans as a function of time (b), the histogram of detected maximum cloud horizontal length from the Ka-SACR as a function of time (c), the histogram of detected cloud top heights from the Ka-SACR as a function of time (d), and number of drops registered by the ARM disdrometer (e).

Figure 9. Temporal evolution of maximum reflectivity for shallow cumuli (a) and the rate of change of maximum reflectivity (b) using a one-minute averaging window as a function of the mean maximum reflectivity over the segment where the rate of change was computed for small shallow cumulus clouds over SGP on May 25, 2011. Respective calculations for median reflectivity are shown in panels (c) and (d). For (b) and (d) color

code indicates the maximum distance between the cloud element outer edge and the radar location [km].

Figure 10. Maximum deviation of the radar scan angle from the wind direction so that the radar measures variables within a homogeneous volume of 50 m diameter as a function of wind speed and cloud lifetime. The area in the top right corner delimitated by the black thick line represents the region where clouds cannot be observed given their time required to sample their full lifecycle, the wind speed, and the domain size.

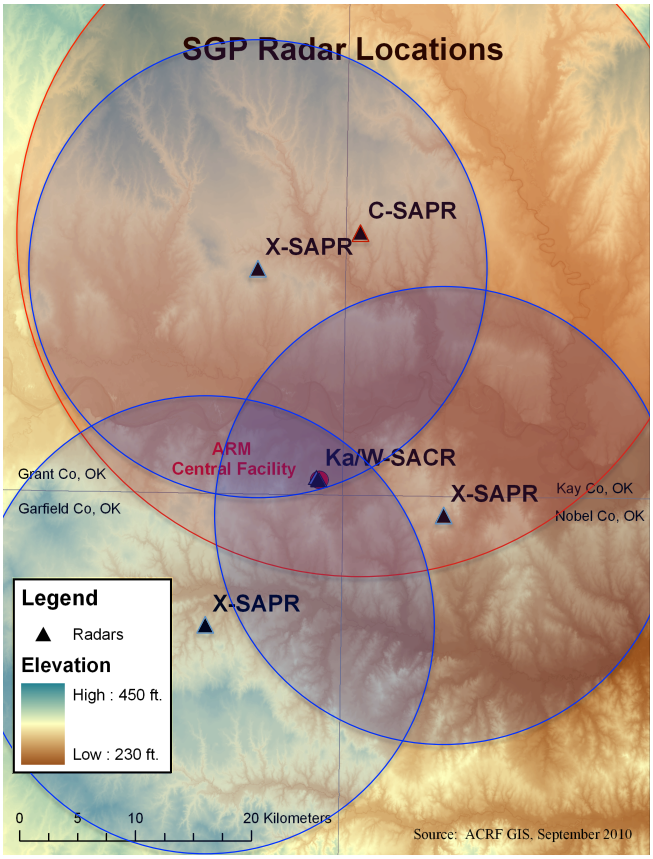

Figure 1. Map showing the heterogeneous ARM radar network at the SGP facility. Blue rings indicate a 20 km radius around each X-band radar and red ring indicates a 30 km radius around the C-band radar.

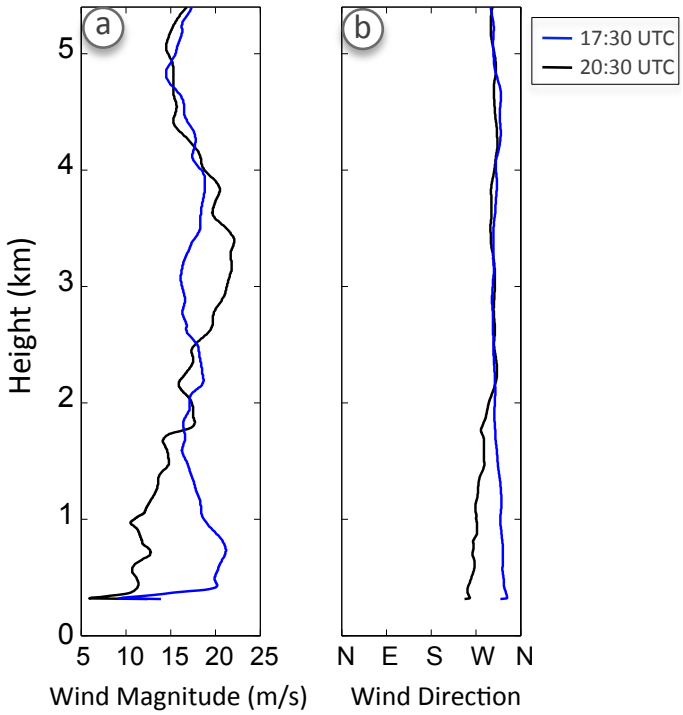

Figure 2. Wind magnitude (a) and direction (b) from radiosonde observations at SGP – CF at 1730 UTC (blue) and 2030 UTC (black) on 25 May 2011.

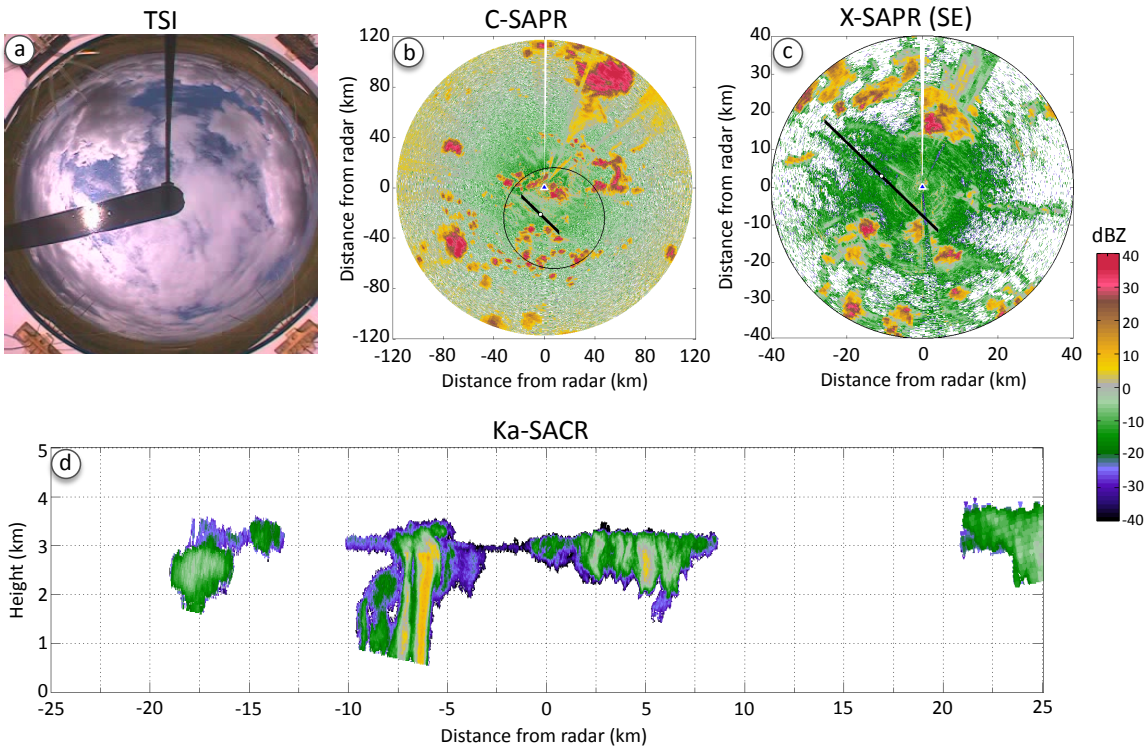

Figure 3. Hemispherical view of the cloud field at the Central Facility from the Total Sky Imager (a), reflectivity from the C-SAPR at 2011 UTC (b), X-SAPR at 2010 UTC(c) PPI scan at 1.2° and 1.5° respectably and from Ka-SACR AW-RHI scan at 2010 UTC (d) on 25 May 2011 when weak non-precipitating cloud were present over the Central Facility. Blue triangle represents the location of the radar and white dot represents the location of the Central Facility; on panels (b) and (c) black line represents the SACR scan and black circle represents the domain where SE X-SAPR data are collected. Orientation in panel (d) is NW on the right and SE on the left.

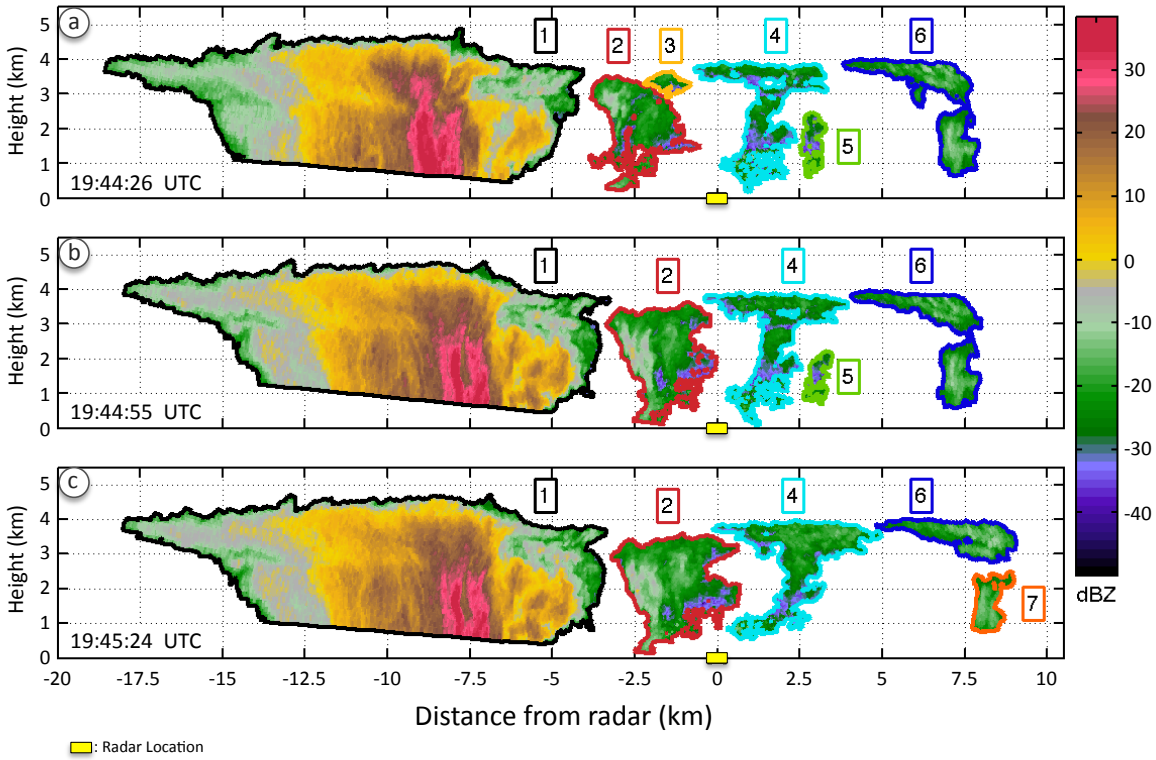

Figure 4. Reflectivity from three consecutive Ka-SACR along-wind scans from 19:44 to 19:45 UTC (shaded) and cloud's identification number documented by the CITA (Contour). Radar location is depicted by the yellow rectangle and the time of each scan is indicated in the bottom left sector of each sub-panel.

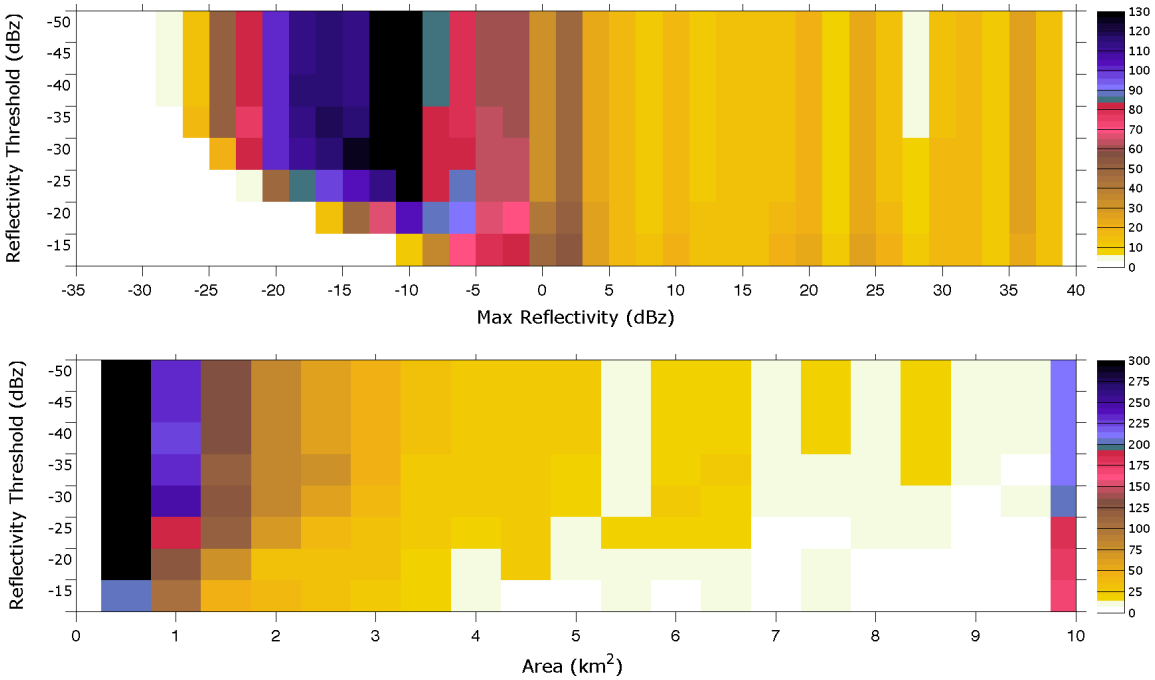

Figure 5. Maximum reflectivity frequency (bin: 2 dB, upper panel) and cloud area cross-section frequency (bin: 0.5 km2, lower panel) for different reflectivity detections threshold in the Cloud Identification and Tracking Algorithm for the 25th May 2011 case.

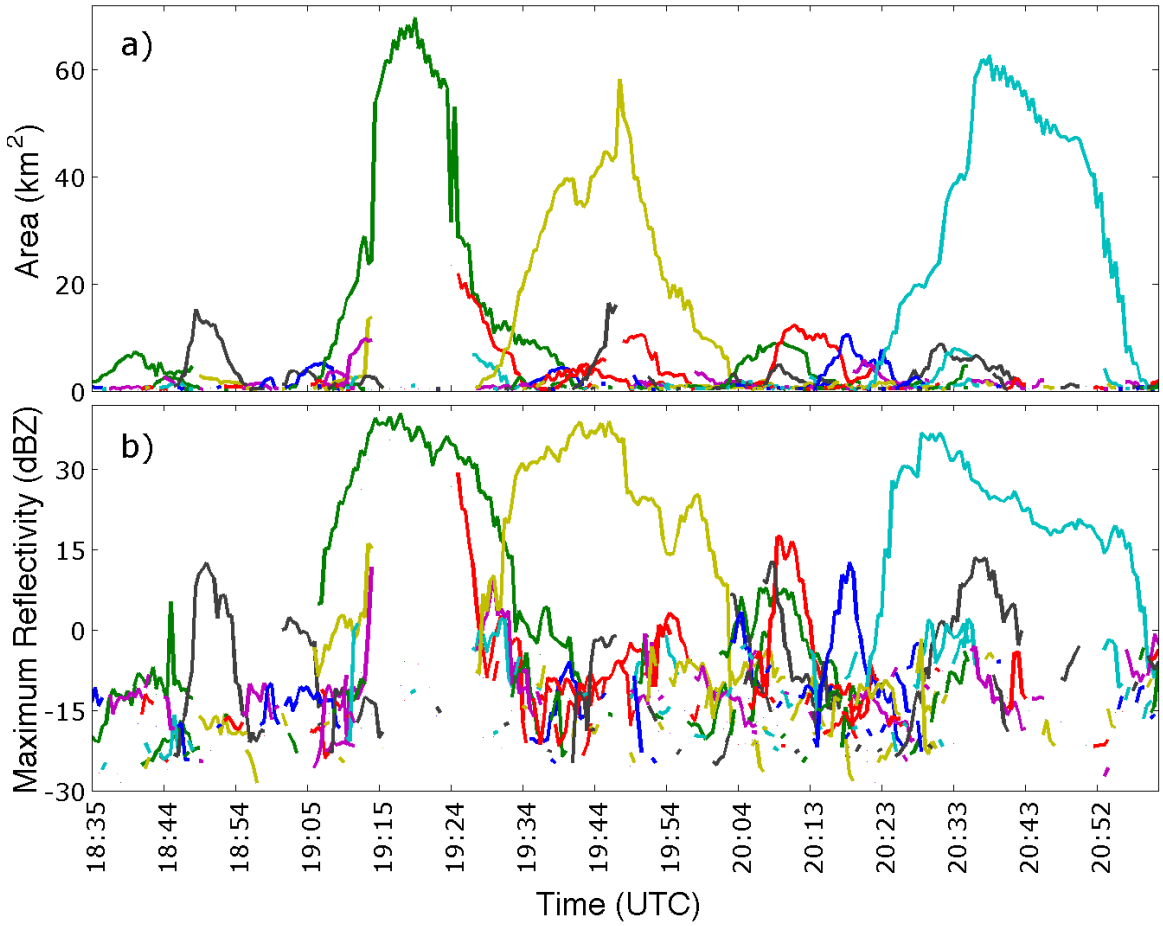

Figure 6. Cross-sectional area (a) and maximum reflectivity (b) as a function of time for every element detected by the CITA on 25 May 2011 during the 2.5-hour window. Colors represent individual clouds tracked by CITA.

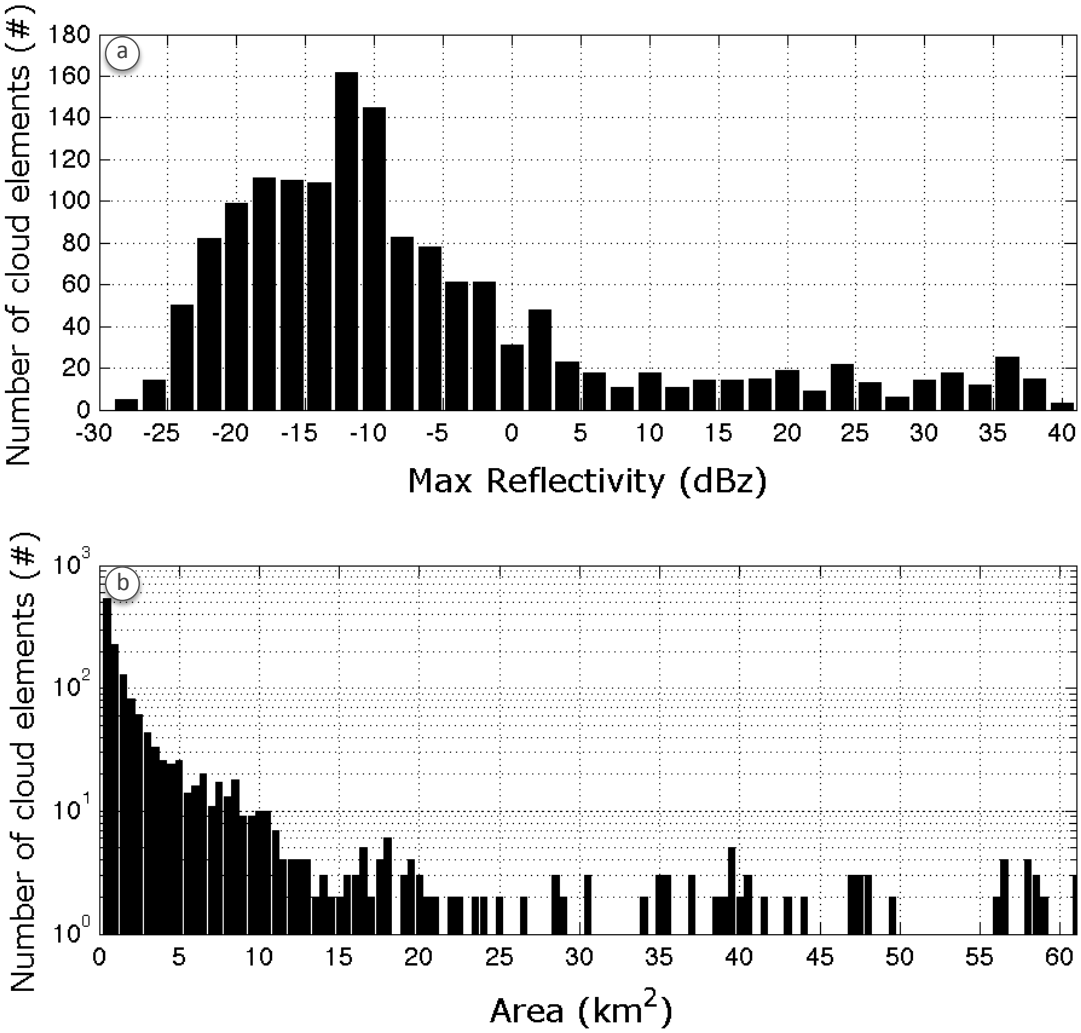

Figure 7. Histogram of maximum reflectivity (a) and area (b) of all cloud elements detected by CITA for the 25 May 2011 case.

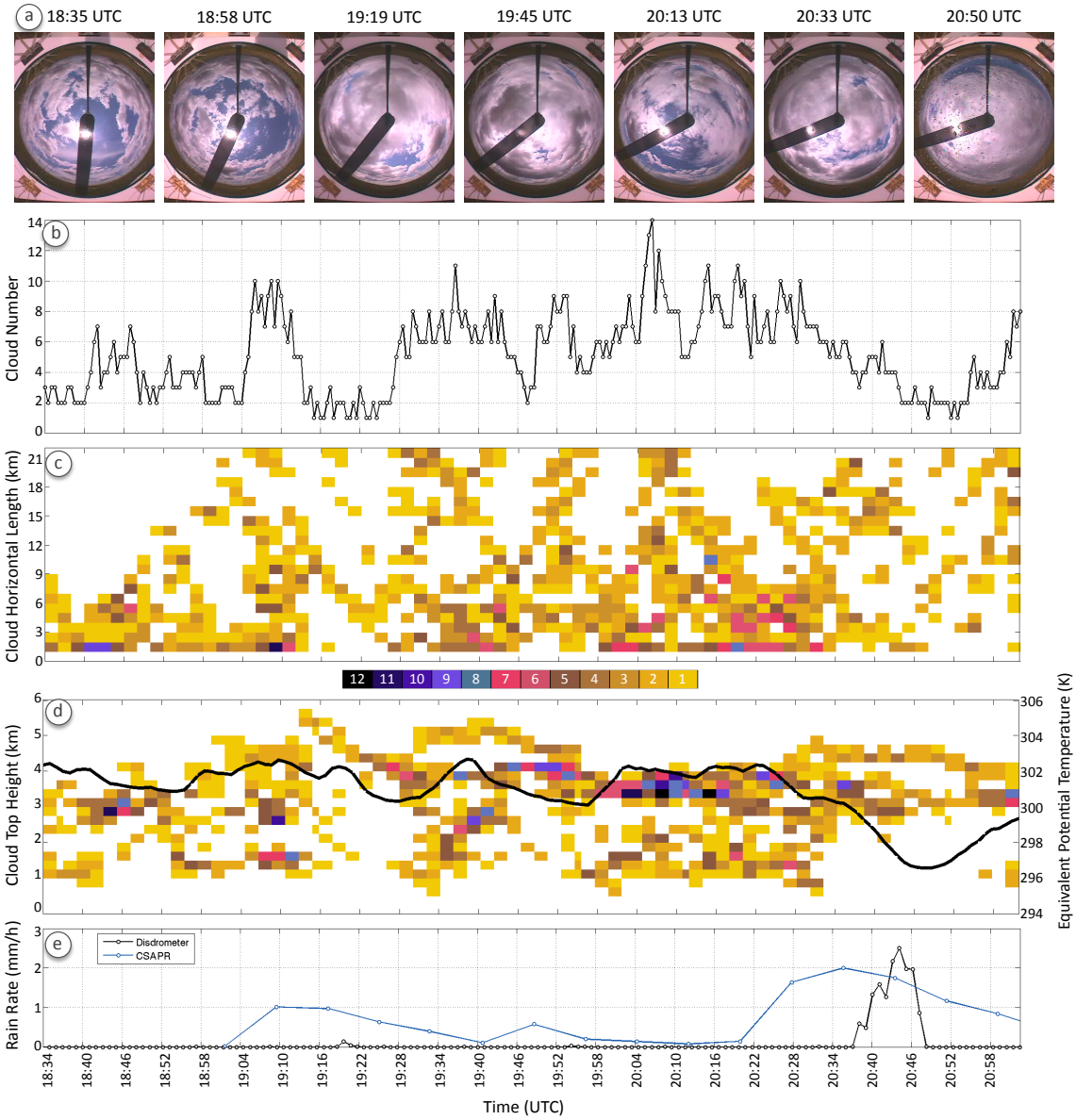

Figure 8. A sequence of TSI images during the 2.5-hour long observing period (a), the number of cloud elements observed in the Ka-SACR AW-RHI scans as a function of time (b), the histogram of detected maximum cloud horizontal length from the Ka-SACR as a function of time (c), the histogram of detected cloud top heights from the Ka-SACR and equivalent potential temperature as a function of time (d), and rain rate estimations from the CSAPR and the ARM disdrometer (e).

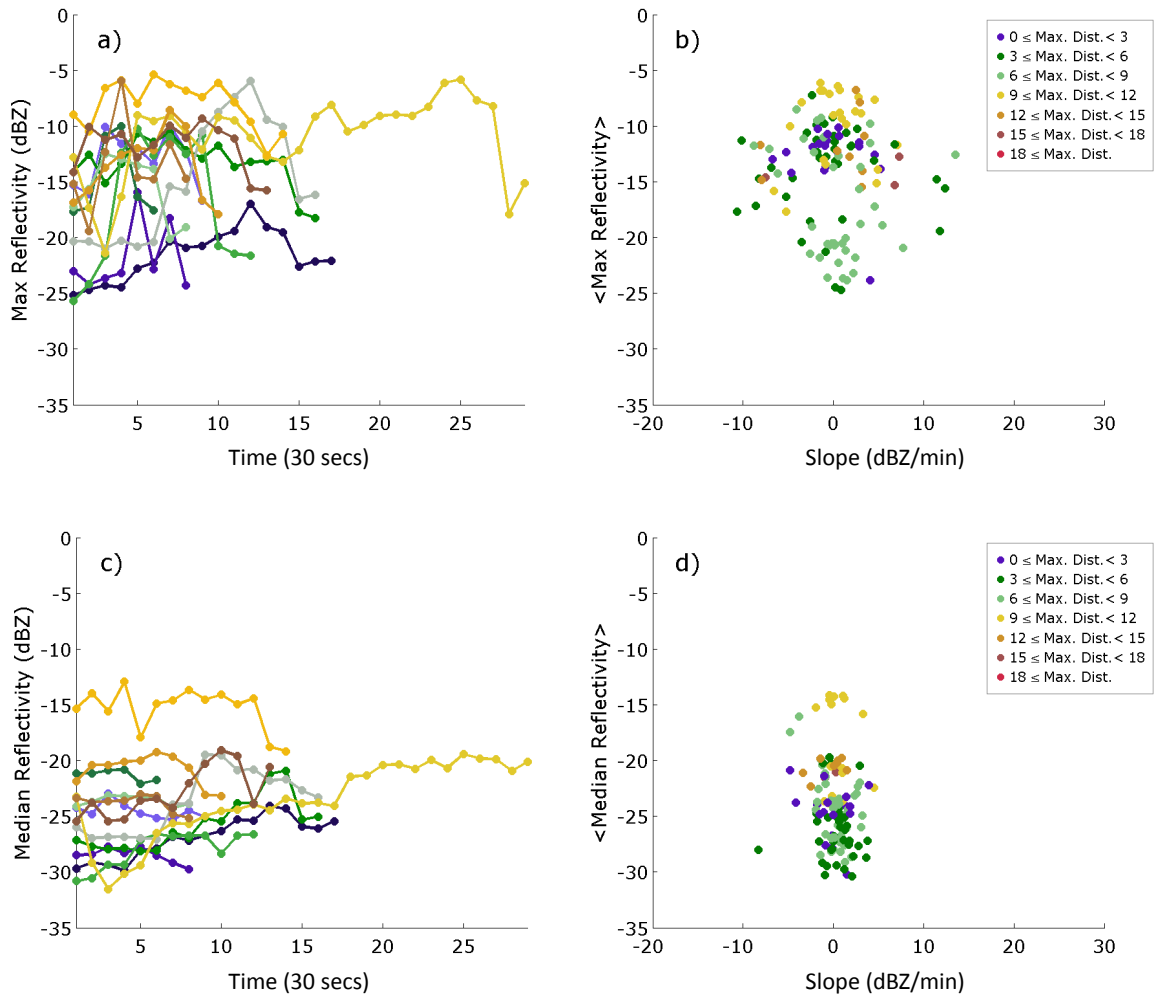

Figure 9. Temporal evolution of maximum reflectivity for shallow cumuli (a) and the rate of change of maximum reflectivity (b) using a one-minute averaging window as a function of the mean maximum reflectivity over the segment where the rate of change was computed for small shallow cumulus clouds over SGP on May 25, 2011. Respective calculations for median reflectivity are shown in panels (c) and (d). For (b) and (d) color code indicates the maximum distance between the cloud element outer edge and the radar location [km].

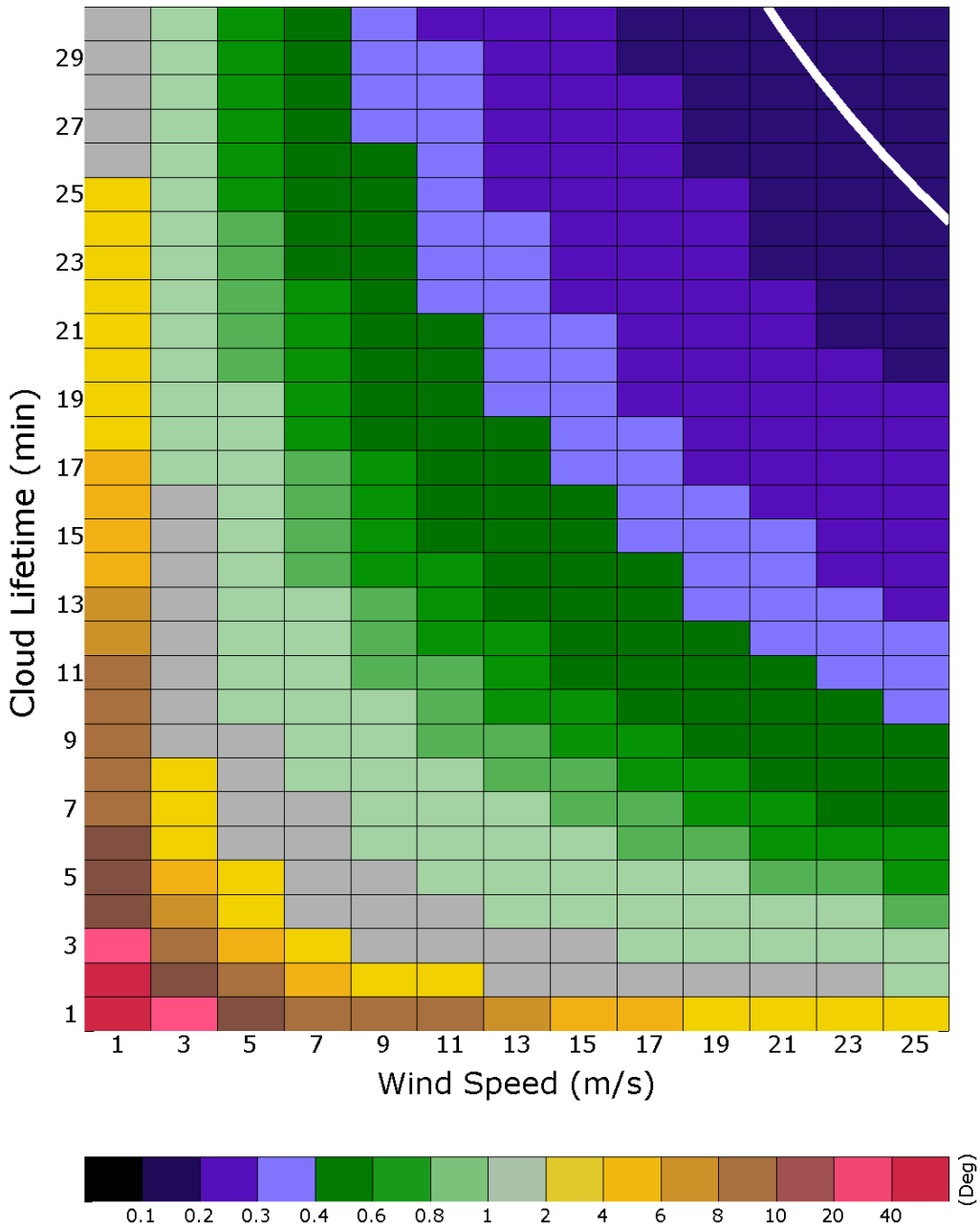

Figure 10. Maximum deviation of the radar scan angle from the wind direction so that the radar measures variables within a homogeneous volume of 50 m diameter as a function of wind speed and cloud lifetime. The area in the top right corner delimitated by the white thick line represents the region where clouds cannot be observed given their time required to sample their full lifecycle, the wind speed, and the domain size.